Journal of Materials Research and Technology 29 (2024) 1102–1117

Contents lists available at ScienceDirect

Journal of Materials Research and Technology

journal homepage: www.elsevier.com/locate/jmrt

Multi-response optimization of M2 steel coatings deposited by co-axial laser cladding on A2 steel tool surfaces

Junfeng Yuan [a,b,*], Heran Geng [a], Marco Alfano [b,c]

[a] School of Mechatronic Engineering, China University of Mining and Technology, Xuzhou 221116, China
[b] Department of Mechanical and Mechatronics Engineering, University of Waterloo, 200 University Avenue West, Waterloo, ON N2L 3G1, Canada
[c] Dipartimento di Scienze e Metodi dell'Ingegneria, Università di Modena e Reggio Emilia, Via Amendola 2, Padiglione Morselli, Reggio Emilia 42122, Italy

ARTICLE INFO

Handling editor: L Murr

Keywords:
Laser cladding
AISI M2 steel
Process optimization
TOPSIS-GRA

ABSTRACT

Laser cladding is a highly effective technique used in additive manufacturing to enhance the surface properties of workpieces. It is employed to improve wear resistance, corrosion resistance, and high-temperature resilience of materials. This study explores the utilization of laser cladding technology to repair the surface of AISI A2 tool steel by applying a coating of M2 steel. Sixteen experiments were designed using an orthogonal methodology to investigate the intricate relationship between various processing parameters, including laser power, scan speed, powder feed rate, and overlapping ratio. These parameters were examined in conjunction with key mechanical properties of the coating, such as micro-hardness, friction-wear characteristics, and shear bond strength.

Additionally, analytical techniques such as Scanning Electron Microscopy (SEM), Energy Dispersive Spectroscopy (EDS), and X-ray Diffraction (XRD) were employed to gain insights into the microstructure of the coatings and elucidate the underlying failure modes. Shear testing of the coatings indicated a tendency towards a brittle fracture mode within the coating, with the dominant wear mechanism involving a combination of abrasive and oxidative wear.

Finally, a TOPSIS-Grey Relational Analysis (GRA) method was utilized to identify the optimal process parameters. These optimal parameters were determined to be a laser power of 1200 W, a scan speed of 5 mm/s, a powder feed rate of 14 g/min, and an overlapping ratio of 30 %. Subsequent validation experiments carried out with these parameters demonstrated superior performance compared to the optimal group identified in the orthogonal experiment.

1. Introduction

During the tool machining process, AISI A2 tool steel is susceptible to wear and plastic deformation when employed as a mold, significantly impacting the mold's lifespan and jeopardizing forming precision, resulting in substantial cost losses. Surface modification techniques offer an effective means of enhancing the mold's lifespan [1,2]. Among these techniques, laser cladding stands out as an excellent option [3]. It involves the rapid melting of alloy powders or metal wires onto the surface of various materials using a high-power laser beam, creating a high-performance cladding layer upon cooling [4,5]. Laser cladding has found successful applications in aerospace, the automotive industry, tool manufacturing, surface strengthening, and repair, among other fields [6]. Studies have proven its capability to significantly improve the wear resistance and hardness of mold material surfaces [2].

Numerous investigations have delved into the performance of laser-cladded coatings under diverse process parameters using experimental design techniques, aiming to determine the ideal process configurations for attaining optimal performance. Lian et al. [7] employed the orthogonal experimental design method to investigate the relationship between process parameters and the micro-hardness, wear resistance, and cladding efficiency of 316L stainless steel coatings prepared by laser cladding. Their research yielded the optimal process parameters that could afford the best performance. In another study, Xi et al. [8] examined the influence of laser power on the micro-hardness and wear resistance of YCF102 coatings prepared by laser re-melting. The results revealed that appropriate laser power effectively reduced the number of defects in the coating, leading to a dense microstructure and improved mechanical properties. Yuan et al. [9] utilized a high-speed laser cladding to prepare Ni45 coatings on AISI 1045 substrates. Thinner and lower-roughness coatings with compact and refined microstructures

* Corresponding author. School of Mechatronic Engineering, China University of Mining and Technology, Xuzhou 221116, China.
E-mail addresses: yuanjfacademia@outlook.com, yuanjf@cumt.edu.cn (J. Yuan).

https://doi.org/10.1016/j.jmrt.2024.01.087
Received 24 November 2023; Received in revised form 8 January 2024; Accepted 10 January 2024
Available online 14 January 2024

Nomenclature

List of symbols

LP	laser power (W)
SS	scan speed (mm/s)
PF	powder feed rate (g/min)
OR	overlapping ratio (%)
x_{ij}	original values of the responses (−)
SNR	signal-to-noise ratio of the responses (−)
ε	volume wear rate (μm^2/N)
F	applied force (N)
f	friction frequency (Hz)
t	friction time (s)
S	wear scar area (μm^2)
SNR_L	larger-the-better response (−)
SNR_S	smaller-the-better response (−)
SNR_N	nominal-the-best response (−)
x_{ij}	performance value (−)
a	mean result for each group under the same response type (−)
X_{ij}	evaluation matrix (−)
Z	normalization matrix (−)
Z^0	ideal target sequence (−)
ζ_{ij}	grey relational coefficient (−)
ξ	distinguishing coefficient (−)
w_j	weight assigned to the jth response (−)
d_i^+	ideal best solution (−)
d_i	ideal worst solution (−)
s_j^+	ideal best solution of the jth experiment (−)
s_j	ideal worst solution of the jth experiment (−)
c_i	score of the ith experiment (−)

were produced by this method, while their corrosion and wear resistance improved with increasing the cladding speed. Lin et al. [10] investigated the influence of different TiB_2 fiber diameters and laser power on the resulting microstructure of TiB_2 powder cladding on TC_4 titanium alloy surfaces. The results demonstrated that high aspect ratio TiB fibers were capable of enhancing the micro-hardness and wear resistance of the cladding layer, which was formed under a TiB_2 diameter of 0.5 μm and suitable laser power (>2.5 kW). In the study by Yu et al. [11], the effect of laser cladding process parameters on the phase composition, microstructure, and friction-wear performance of single-phase NiAl coatings was investigated. The results indicated that low laser power density produced excellent coatings, i.e., denser microstructure, a lower friction coefficient, and a lower wear rate. Additionally, Lian et al. [12] explored the influence of process parameters on the micro-hardness and wear resistance of Ni-based alloy-TiC composite cladding layers. By using response surface methodology, they established a mathematical model and obtained optimal process parameters, resulting in a significant improvement in wear resistance (~six-fold) and a reduction in wear volume (~84 %) of the coatings.

The above studies highlighted the excellent wear and mechanical performances of laser-cladded coatings made of 316L steel, Ni- and Ti-based alloys. However, because of its exceptional friction-wear attributes, AISI M2 high-speed steel is a potential candidate for applications involving the enhancement and restoration of high-temperature molds used in hot working processes [13]. This steel demonstrates remarkable resistance to wear, excellent tempering stability, and a high threshold for plastic deformation. Additionally, its micro-hardness displays minimal susceptibility to fluctuations in temperature [14]. Nonetheless, the optimization of performance and the quality of coatings critically depend on the precise selection of process parameters. Despite the promising traits of M2 steel, there remains a scarcity of research concerning its practical implementation within the realm of laser cladding.

The main aim of the present study is to bridge this existing gap by investigating the friction-wear performance of M2 coatings deposited on A2 steel substrates using laser cladding. Phase composition, microstructure, and element distribution were analyzed utilizing an X-ray diffractometer (XRD), scanning electron microscopy (SEM), and energy-dispersive spectroscopy (EDS), allowing the wear mechanism and fracture behavior of the coating to be determined. More importantly, a thorough analysis was conducted to comprehend the intricate relationship between performance metrics and the experimental variables inherent in the process. Specifically, we engaged in uncovering the impact of various process parameters, such as laser power (LP), scan speed (SS), powder feed rate (PF), and overlapping ratio (OR). These parameters were carefully examined in relation to their effects on crucial performance indicators, including microhardness and the friction-wear characteristics of the coatings.

Additionally, it is crucial to acknowledge that the durability of the mold relies on two fundamental factors: the mechanical properties of the coating and the bond strength between the coating and the substrate [2]. Past research has convincingly illustrated instances where the improper selection of process parameters led to coatings with a microstructure prone to detachment and fracture [15–18]. In consideration of these points, we introduced an extra performance measure, namely bond strength, to assess the quality of the generated coatings. This metric, which is determined by the maximum load achieved in compression-shear experiments [17], offers further insights into the coatings' overall quality.

Regarding process parameters, we aim to determine the optimal settings for each performance index. However, when dealing with multiple responses, it arises a necessity to identify the optimal set of parameters through multi-objective optimization techniques. Given the rapid advancements in the computer industry, a plethora of multi-objective optimization methods have emerged. Notably, Grey Relational Analysis (GRA) has gained substantial traction as an exceptional approach for optimizing laser cladding process parameters [19,20]. Nonetheless, this method has encountered critique due to its subjective assignment of weights to individual responses [21]. To tackle the challenge of weight assignment, several scholars have employed GRA to derive weights and have performed a comprehensive assessment utilizing the so-called TOPSIS (Technique for Order Preference by Similarity to Ideal Solution) method [22,23]. TOPSIS is rooted in measuring the similarity to ideal solutions to establish a technical order of preference. This integrated approach enhances the reliability of results and has found effective applications across diverse problem domains, such as ranking weaponry and evaluating industries [21–23]. Therefore, the TOPSIS-GRA method was employed herein to evaluate and determine the optimal process parameters of laser cladded M2 coatings. Finally, validation experiments were conducted using the optimal parameters.

2. Materials and methods

2.1. Materials and laser cladding equipment

The materials used in this study consisted of AISI A2 tool steel substrates measuring 100 x 100 × 10 mm^3. For the fabrication of coatings, the AISI M2 high-speed steel powder material was employed. The powder exhibited a spherical morphology, with particle sizes ranging from 45 to 105 μm, conforming to a normal distribution. Prior to the laser cladding process, the powder underwent a vacuum drying treatment at a temperature of 100 °C for 2 h. Subsequently, it was stored in a vacuum. The substrate surface underwent polishing using a manual

grinder to remove oil stains. Afterward, the substrate surface was meticulously cleaned with anhydrous ethanol. Both AISI A2 tool steel and AISI M2 high-speed steel materials were provided by Jiangsu Weilali New Material Technology Co., Ltd., and their compositions can be found in Table 1.

The laser cladding system used in this study is illustrated in Fig. 1(a). It consists of several components, including a laser generator, a laser head, a robotic arm, a water cooler, a powder feeder, a control system, and an operating handle. The laser generator was provided by Wuhan Raycus Fiber Laser Technologies Co., Ltd. It is equipped with a high-power continuous fiber laser capable of generating a maximum average output power of 3.3 kW and operates within a wavelength range of 900–1200 nm. It's important to note that the laser spot diameter remained fixed at 2 mm, with a constant defocus distance of 12 mm. The powder was delivered coaxially, and to prevent oxidation, argon gas was used as both the shielding and carrier gas, with a gas flow rate of 4 L/min. The cladding layer preparation process can be observed in Fig. 1 (b), where high-intensity laser energy melts the powder onto the pre-processed upper surface of the substrate, resulting in the creation of the coating.

2.2. Micro-hardness, wear and friction measurements

After processing, the coated specimens were divided into individual blocks using electrical discharge wire cutting technology. The blocks were then utilized as samples for micro-hardness testing. Each sample had cross-sectional dimensions of 25 × 11 mm^2, while the coating thickness was reduced to 1 mm through milling. Subsequently, the cut surfaces of the micro-hardness samples underwent sequential polishing (#100, #400, #800, #1200, #1500, and #2000 sandpapers) to achieve a smooth surface finish. Final polishing was then performed using a polishing cloth.

Micro-hardness testing of the sample cross-sections was carried out using the HVS-1000A micro-hardness tester (manufactured by Laizhou Huayin Testing Instrument Co., Ltd.). A force of 5 N was applied with a dwell time of 10 s during loading. Micro-hardness experiments were conducted at 14 distinct points. The measurements started from the upper edge of the coating and were spaced at intervals of 0.1 mm, continuing down to 1 mm beneath the assumed substrate/coating interface. Each horizontal line underwent three measurements, spaced with a gap of 0.7 mm between them. The average result of the three points on the same horizontal line was considered as the final value for that specific line.

The friction-wear samples were also prepared utilizing electrical discharge wire cutting technology, with a sample size of 25 × 25 mm^2 and a coating thickness of 1 mm. The coating surface was polished to ensure consistent measurements throughout the experiments [11]. The dry sliding test was performed using the CETR UMT-3 wear tester (CETR Friction and Wear Testing Machine, Bruker Corporation, USA). The friction mode was reciprocating dry friction, and the grinding ball was a ZrO_2 ceramic ball with a diameter of 3 mm. The loading force, single friction stroke, friction frequency, and friction time were held constant at 30 N, 5 mm, 1 Hz, and 30 min, respectively. The force sensor was utilized to monitor the variation of the friction coefficient (CoF). The average coefficient of friction was calculated and adopted to characterize the performance of each sample.

The three-dimensional morphology and the mean area of the wear tracks were determined using a digital microscope (DSX1000, Tokyo Olympus Corporation). The volume wear rate of the sample was calculated using the following equation:

$$\varepsilon = \frac{S}{2Ftf} \tag{1}$$

where F is the applied force (N), f is the friction frequency (Hz), t represents the friction time (s), and S represents the wear scar area (μm^2). Upon examining the equation, it becomes evident that only S varies, while the other parameters in our experiments remained constant. As a result, this study employs the wear scar area instead of the volume wear rate to effectively characterize the coating's wear performance.

2.3. Assessment of bond strength

To evaluate the bond strength, we prepared test specimens using a custom-made mold and in accordance with the ASTM B898 standard [24]. Specifically, we applied coating strips measuring 16 x 1.5 × 1 mm^3 onto steel blocks and subjected them to shear loading, as depicted in Fig. 2. Notably, we controlled the coating thickness at 1 mm through milling.

The shear tests were conducted using a universal testing machine (Changchun Research Institute for Testing Machines Co., Ltd., China) with a maximum testing force capacity of 250 kN. The displacement rate was set at 4 mm/min, and a force sensor continuously recorded the force-displacement curve throughout the coating failure process. As reported elsewhere, the bonding strength between the coating and the substrate can be characterized using the maximum shear force at the point of coating fracture [17]. This specific parameter represents the force needed to shear the coating away from the substrate and offers valuable insights into the bond strength for varying process parameters.

2.4. Analytical analysis methods

The micro-hardness samples, friction-wear samples, and shear samples were further examined through an array of advanced analytical techniques, including Field Emission Gun Scanning Electron Microscopy (SEM; FEI Quanta 250) with an Energy-Dispersive X-ray Spectroscopy (EDS), and X-ray Diffraction (XRD; Bruker D8 advanced). Collectively, these analyses are aimed at providing a comprehensive view of the microstructure, elemental makeup, and phase characteristics of the coatings. In particular, through SEM, we delved into the microstructure of the samples, capturing detailed images that unveil the surface morphology and structural features at a microscale level. In tandem with SEM, EDS was used to gain insights into the elemental composition of the coatings, enabling us to identify and quantify the constituent elements present in the coatings. Furthermore, the XRD tests were executed to gain a precise understanding of the crystalline phases and crystallographic structure of the coatings, with a current of 30 mA, a voltage of 40 kV, a scanning speed of 4°/min and a scanning range from 20° to 90°.

2.5. Design of experiments

Conducting performance tests on coatings can be a resource-intensive and expensive undertaking. To streamline the experimentation process, the orthogonal experimental design approach has demonstrated its effectiveness in reducing both time and costs [25]. Thus, for the present study, we opted to employ the orthogonal experimental design method. To optimize the laser cladding process, we elected four main process parameters: laser power (LP), scan speed (SS), powder

Table 1
Chemical composition of the materials involved in the present study (wt.%).

Steel type	C	Si	Mn	Cr	P	S	W	V	Mo	Fe
A2	1.00	0.30	0.60	5.00	0.03	0.03	–	0.25	1.00	bal.
M2	0.97	0.20	0.20	4.11	–	–	6.30	1.80	4.90	bal.

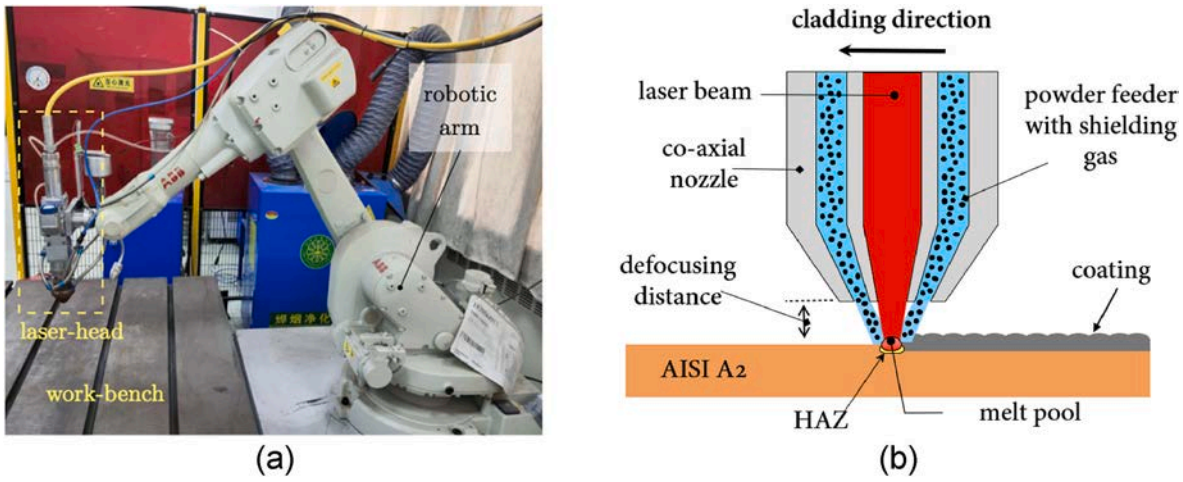

Fig. 1. Laser cladding equipment employed in the current study. (a) Robotic arm with laser head. (b) Schematic of the laser head with co-axial powder feeder.

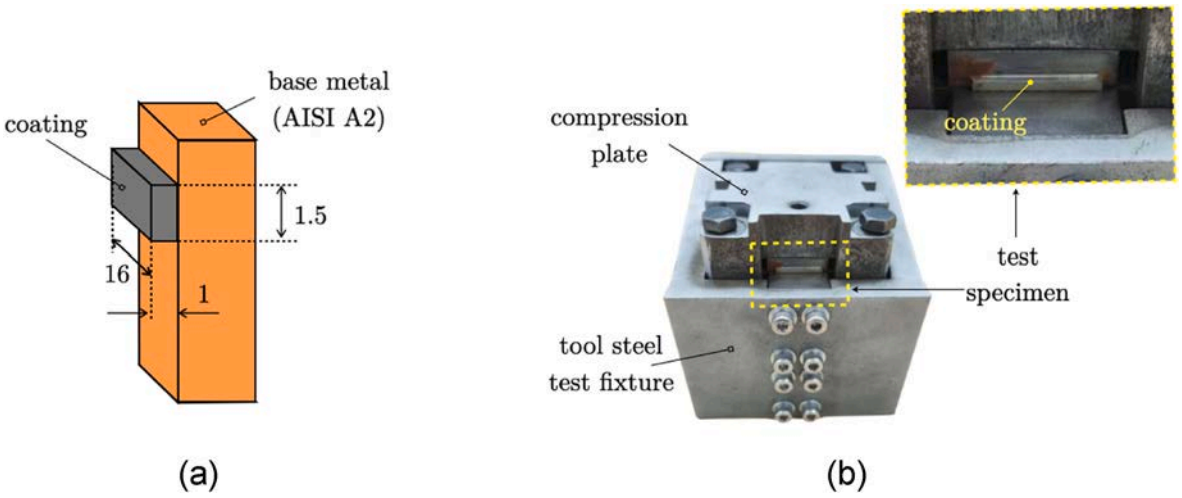

Fig. 2. Set-up employed for shear tests. (a) Schematic of the test specimen. (b) Actual specimen within the sample holder before being connected to the loading frame of the testing apparatus. The quoted dimensions are [mm] (not to scale).

feeding rate (PF), and overlapping ratio (OR). Each of these parameters was varied across four levels, as outlined in detail in Table 2.

Notice that the range of experimental variation was selected based on previous studies [1,26]. Subsequently, we performed an L16 (4^4) orthogonal experimental design, generating a set of 16 distinct process parameter combinations, which are itemized in Table 3.

2.6. Procedure employed for multi-response optimization

Within orthogonal experiments, the analysis of variance (ANOVA) and signal-to-noise ratio (*SNR*) approaches stand as prevalent tools for data interpretation. Based on the probability (P-value) of different process parameters, ANOVA determines the significance of each process parameter on the measured response. A P-value less than 0.05 implies that the parameter has a significant effect on the response.

Table 2
Orthogonal experimental design method.

Variable	Level 1	Level 2	Level 3	Level 4
Laser power, LP [W]	1200	1400	1600	1800
Scan speed, SS [mm/s]	5	6	7	8
Powder feed rate, PF [g/min]	12	14	16	18
Overlapping ratio, OR [%]	30	40	50	60

Table 3
Orthogonal array L16 (4^4) matrix.

Sample #	SS [mm/s]	LP [W]	PF [g/min]	OR %
1	8	1200	16	30
2	8	1400	14	40
3	8	1600	16	50
4	8	1800	18	60
5	7	1200	14	50
6	7	1400	12	60
7	7	1600	18	30
8	7	1800	16	40
9	6	1200	16	60
10	6	1400	18	50
11	6	1600	12	40
12	6	1800	14	30
13	5	1200	18	40
14	5	1400	16	30
15	5	1600	14	60
16	5	1800	12	50

SNR is used as a measure of process robustness in orthogonal experiments and is categorized into three types: larger-the-better response (SNR_L), smaller-the-better response (SNR_S), and nominal-the-best

response (SNR_N). The equations used to calculate the *SNR* are given as follows [27,28]:

$$SNR_L = -10\log\left(\frac{1}{n}\sum_{i=1}^{n}\frac{1}{x_{ij}^2}\right) \tag{2}$$

$$SNR_S = -10\log\left(\frac{1}{n}\sum_{i=1}^{n}x_{ij}^2\right) \tag{3}$$

$$SNR_N = -10\log\left(\frac{1}{n}\sum_{i=1}^{n}\left(x_{ij}-a\right)^2\right) \tag{4}$$

where n (=16) represents the number of experimental groups, x_{ij} represents the measured response data in a given experiment and a is the mean result for each group under the same response type. In this work, microhardness and bond strength were categorized as 'larger-the-better' data, and their *SNR* ratios were calculated using Eq. (2). Wear scar area and CoF were categorized as 'smaller-the-better' data, and their *SNR* values were obtained using Eq. (3).

ANOVA and *SNR* methods are valuable tools for determining optimal parameters for individual performance metrics, but they fall short in determining the process parameters that can yield the best overall performance [29,30]. Traditional grey relational analysis (GRA), while capable of achieving multi-objective optimization, does not consider the weights of each response, potentially affecting the reliability of the evaluation results and the search for optimal parameters [18]. To address this issue, a hybrid approach is employed herein that combines GRA and the Technique for Order of Preference (TOPSIS) methods. Such an approach is used for multi-criteria decision-making and is particularly useful when dealing with complex and uncertain data [21]. Therefore, microhardness, bond strength, wear scar area, and CoF were used as response metrics, and the TOPSIS-GRA method was applied for comprehensive performance evaluation.

The TOPSIS-GRA method integrates the TOPSIS method, which ranks alternatives based on their proximity to the ideal and worst solutions, with Grey Relational Analysis (GRA), which assesses the similarity between alternatives and the ideal solution using Grey Relational Coefficients. This combination allows decision-makers to consider both the proximity to the ideal solution and the degree of similarity to it when selecting the best alternative for multi-objective optimization problems. The TOPSIS-GRA method implemented herein consists of the following seven steps:

Step #1. An evaluation matrix X_{ij} is created where each element represents the performance value of attribute j (jth response) of alternative i (ith experimental run), with $i = 1, \ldots, n$, $j = 1,2, \ldots, m$ ($m = 4$, $n = 16$). The raw data is categorized into maximization and minimization types to obtain the matrix $Y=(y_{ij})_{nxm}$, where:

$$y_{ij} = \left|x_{ij} - \max_i x_{ij}\right| \tag{5}$$

Step #2. The influence of different units is eliminated through normalization:

$$z_{ij} = \frac{my_{ij}}{\sum_{j=1}^{m} y_{ij}} \tag{6}$$

And the maximum value of each column of $Z=(z_{ij})_{nxm}$ is extracted to form a reference sequence (ideal target sequence) denoted as $Z^0=(z^0(1), \ldots, z^0(m))$.

Step #3. Determination of grey relational coefficient (GRC) for the jth response in the ith experiment:

$$GRC_{ij} = \frac{\min_i\min_j\left|z_{ij}-z_{j_0}\right| + \xi\max_i\max_j\left|z_{ij}-z_{j_0}\right|}{\left|z_{ij}-z_{j_0}\right| + \xi\max_i\max_j\left|z_{ij}-z_{j_0}\right|} \tag{7}$$

where x is the "distinguishing coefficient" that takes values in the range of $0< x < 1$, and in this study, it is set to 0.5 [31].

Step #4. Calculate the response weight. For the jth response:

$$w_j = \frac{\sum_{i=1}^{n}\zeta_{ij}}{\frac{1}{m}\sum_{j=1}^{m}\sum_{i=1}^{n}\zeta_{ij}} \tag{8}$$

where w_j signifies the weight assigned to the jth response.

Step #5. Standardize the positive-normalized matrix Y.

$$s_{ij} = \frac{y_{ij}}{\sqrt{\sum_{i=1}^{n} y_{ij}^2}} \tag{9}$$

Step #6. Define the distance of the ith experiment from the ideal best and worst solutions, respectively:

$$d_i^+ = \sqrt{\sum_{j=1}^{m} w_j\left(s_j^+ - s_{ij}\right)^2} \tag{10}$$

$$d_i^- = \sqrt{\sum_{j=1}^{m} w_j\left(s_j^- - s_{ij}\right)^2} \tag{11}$$

where s_j^+ is the ideal best solution of the jth experiment, and s_j^- is the ideal worst solution, with values being the maximum and minimum of that column, respectively.

Step #7. Calculate the score of the ith experiment as follows:

$$c_i = \frac{d_i^-}{d_i^+ + d_i^-} \tag{12}$$

where c_i represents the score of the ith experiment. A higher score indicates better overall performance for that specific experimental group.

The obtained scores for each group serve as a comprehensive indicator for ANOVA and *SNR* analysis, facilitating the identification of the four process parameters that can simultaneously satisfy the four responses.

3. Results and discussion

3.1. Analysis of micro-hardness test results

As mentioned previously, the current study has considered the following key responses: micro-hardness, bond strength, wear scar area, and the coefficient of friction. The experimental results for each combination of processing variables can be found in Table S1. Besides, representative microhardness test results as a function of position are illustrated in Fig. 3 (the full set is reported in Fig. S1).

From these results, it is apparent that the micro-hardness of the coatings predominantly falls within the range 690–820 $HV_{0.5}$, which is consistent with previous studies [32]. In comparison, the micro-hardness of the substrate exhibits variations spanning 200–300 HV, which highlights the substantial enhancement of micro-hardness afforded by the M2 coating. Both ranges are highlighted in Fig. 3(a). It is worth noting that the hardness decreases as the testing points approach the substrate, with a gradual transition through the

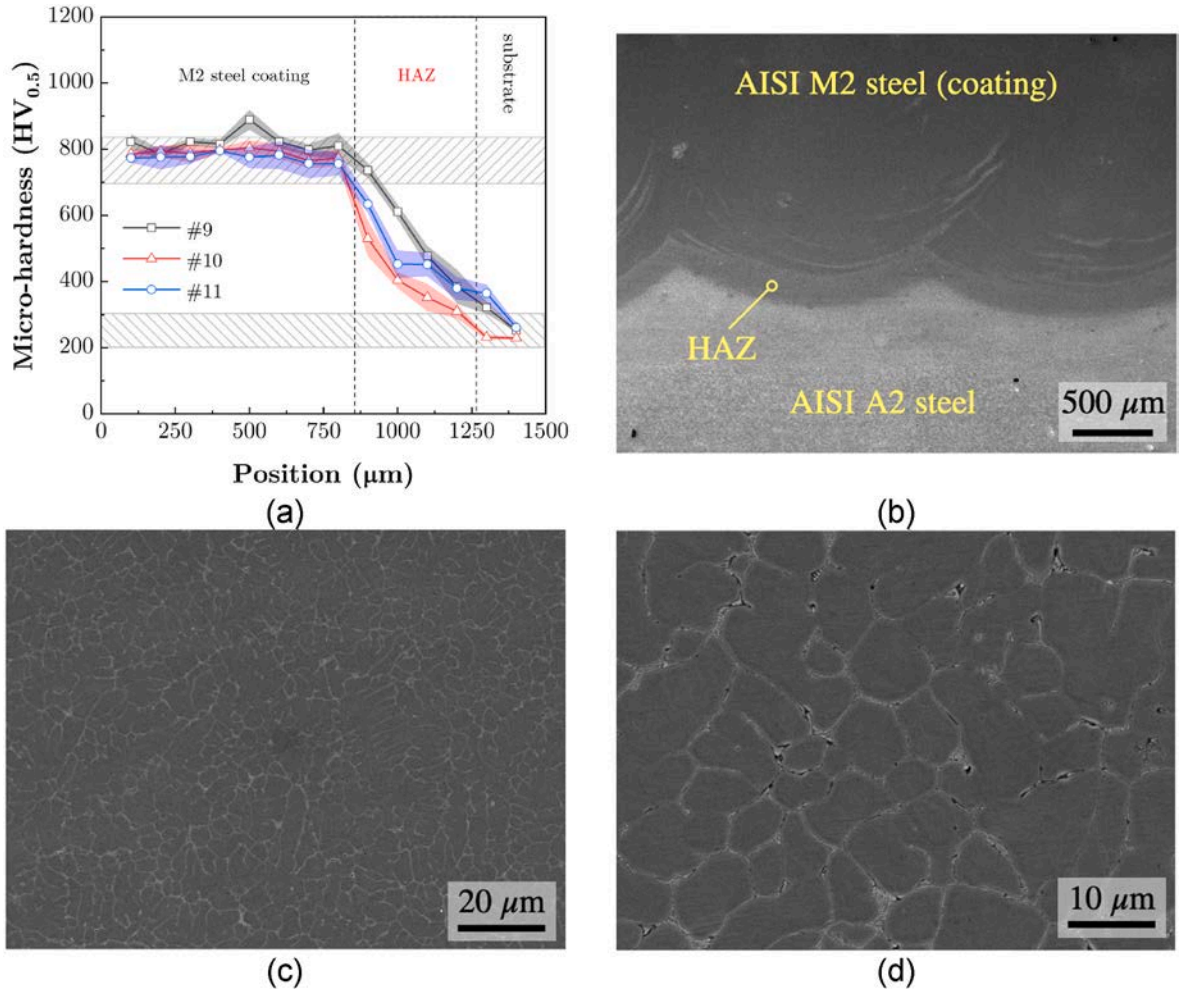

Fig. 3. (a) Typical results of micro-hardness measurements for selected experiments from the Taguchi table. (b–d) SEM cross-sectional observation of the coating (#11).

heat-affected zone (HAZ). The HAZ is the region where substrate and powder material melt together, and as proximity to the substrate increases, the proportion of substrate material rises, contributing to lower micro-hardness values [33].

Microscopic analysis was conducted using scanning electron microscopy (SEM). Prior to imaging, the samples were prepared by subjecting them to etching with "aqua regia". It is important to note that the 16 groups of process parameters outlined in Table 3 were arranged in descending order based on the coating microhardness results. Subsequently, six samples—#3, #11, #6, #8, #13, and #1—were selected for further testing in accordance with the obtained hardness gradient. This method minimizes the number of experiments while emphasizing the variations among different samples. Fig. 3(b) displays SEM micrographs of sample #11 selected from the above group (the complete set is presented in Fig. S2), illustrating the absence of cracks or pores at the interface between the coating and the substrate. This observation corroborates the formation of a strong metallurgical bond, affirming the successful laser cladding of M2 high-speed steel coatings onto the A2 steel. Besides, within the coating area, the high-energy laser process causes the rapid melting and subsequent cooling of the M2 powder. This leads to the development of a finely textured cellular-dendritic solidification structure, which is shown at two distinct magnifications in Fig. 3 (c) and (d). It is important to highlight that the observed decrease in microhardness correlates with an increase in grain size, as illustrated in Fig. S2. This phenomenon indeed results in material softening.

In addition, we performed X-ray Diffraction (XRD) analysis to examine the phase composition of the M2 coating. Sample #11 was once again chosen for this analysis, and the complete set of XRD analyses for the entire group of specimens previously mentioned—#3, #11, #6, #8, #13, and #1—is presented in Fig. S3.

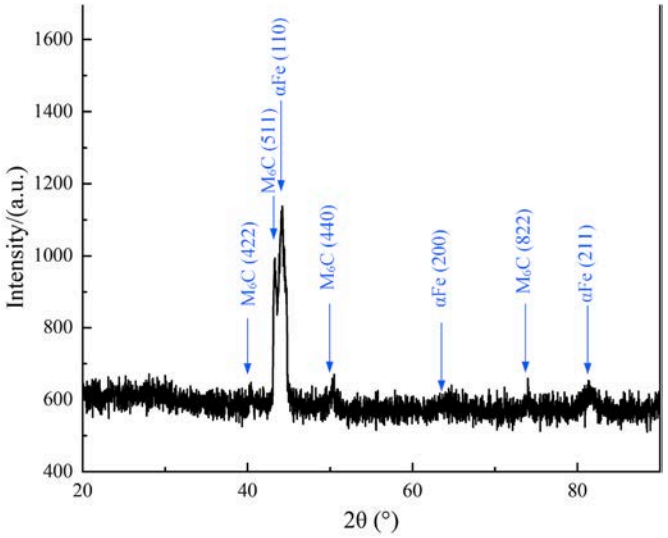

Fig. 4. XRD spectrum of the M2 coating (#11).

As illustrated in Fig. 4, the results of this examination revealed a significant prevalence of M_6C-type Fe_3W_3C carbides (composed with Fe, W, Cr, Mo and V) [13,33]. Moreover, this observation suggests that the cellular-dendritic structure is primarily composed of M_6C-type carbides, which result from the dissolution of primary carbide grains (with varying in size and shape and unevenly distributed) during the solidification process, forming intricate networks of finely dispersed carbides [34].

The presence of these extremely fine carbides, along with substantial quantities of hard elements such as vanadium (V) and tungsten (W), and in combination with the presence of martensitic laths and precipitated carbides, collectively contribute to the increased hardness exhibited by the M2 coating. It is important to note that variations in coating hardness may also potentially arise from the uneven distribution of carbides within the coating area [33,34].

3.2. Analysis of the bond strength

Typical load-displacement curves obtained in shear tests are illustrated in Fig. 5. These plots were adjusted for the take of displays. The remainder of the tests displayed essentially the same trend and were differentiated by the peak load achieved to sever the coating (the full set of results is provided in Fig. S4). Notice that the bond strength was extracted from such results and was represented by the peak load recorded during each test. The results selected for Fig. 5 aim to highlight that there are significant differences in the bond strength among the various experimental conditions, indicating that changes in process parameters have a significant effect on the bond strength.

It should be noted that the load sharply decreases to nearly zero after reaching the peak value, indicating that the coating fracture occurs in a brittle manner. This result contrasts with the research conducted by Xu et al. on laser-cladded IN718 coatings [18], where the load steadily decreased after reaching its peak, as opposed to abruptly dropping to zero. To investigate the phenomenon of coating fracture and examine the factors contributing to variations in bond strength, we employed SEM and EDS techniques to analyze the microstructure and elemental composition of the fracture surfaces.

We restricted the analysis to coatings #4 and #14, i.e, sample #4 exhibited the lowest bond strength, while sample #14 had the highest bond strength. However, the full set of results is reported in Fig. S5.

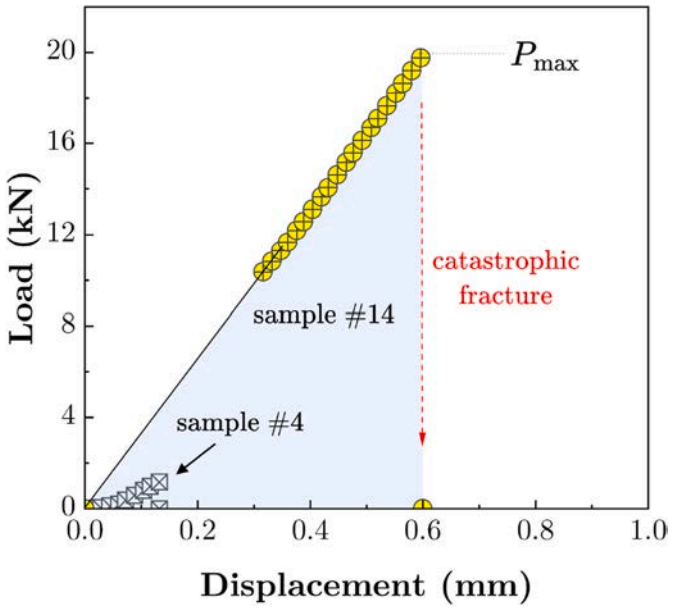

Fig. 5. Reaction force as a function of the machine stroke obtained in shear testing of coatings #4 and #14 (after correction of the take of plays).

Notice that the 16 groups of process parameters were sorted according to the sequence of coating bond strength results from largest to smallest, and then a group of six samples, i.e., #14, #5, #13, #7, #16, and #4, was selected for further analysis.

The fracture surface of sample #4 is shown in Fig. 6(a) and appears relatively flat, characterized by extensive areas with a bright silver metallic sheen, interspersed with large black regions. Notably, the bright silver region closely resembles the color of the substrate, suggesting an inadequate bond between the coating and the substrate. This observation implies the presence of a suboptimal metallurgical connection between the coating and the substrate, which is indicative of a near-interfacial fracture. The presence of black regions may be attributed to extensive oxidation on the substrate's surface. This phenomenon arises from inadequate bond strength, leading to gaps between the substrate and the coating. Consequently, during the cooling process, the absence of protective gas exposes the substrate to oxidation, triggered by the reaction between gases within the gaps and the substrate.

An EDS line scan was conducted on sample #4, as shown in Fig. 6(a) and the resulting chemical composition has been documented in Table 4. The findings corroborate that the elemental makeup differs significantly from that of the coating, with notably low quantities of Mo, W, and V elements, accounting for only 2.44 %, 1.06 %, and 0.15 %, respectively. This suggests that only a limited portion of M2 and the substrate entered into metallurgical bonding, thereby accounting for the reduced bond strength observed with this particular combination of manufacturing process parameters. Moreover, the oxygen content was measured at 24.53 %, confirming the previous speculation about the black regions.

The fracture surface of sample #14, which is shown in Fig. 6(b), did not display any apparent signs of plastic deformation, such as shear lips. This observation suggests that the fracture mode of the coating remains brittle, which aligns with the findings reported in Ref. [26]. Nonetheless, the appearance of these fracture surfaces indicates a transgranular fracture. Further detailed examinations (see Fig. S6) indicated the absence of ductile dimples and the presence of cleavage steps, pointing toward a cleavage fracture mechanism, consistent with previous research [35,36].

To pinpoint the location of fracture, we conducted an EDS line scan also on sample #14, and the results are superimposed in Fig. 6(b) and documented in Table 4. The proportions of Mo, W, and V elements were found to be 6.82 %, 11.01 %, and 3.44 %, respectively, which align with the composition of the coating. Additionally, there was a noticeable reduction in the levels of C and O elements compared to sample #4. This provides confirmation that the cracking initiates from the coating, and the fracture surface primarily comprises M2, supporting the formation of a strong metallurgical bond between the coating and the substrate.

3.3. Analysis of CoF and wear scar area

Typical results of friction tests process curves for each sample are shown in Fig. 7. During the initial stage of the wear process the contact area between the sample and the grinding ball is small, leading to significant fluctuations in CoF due to higher contact stresses. However, as the contact area increases, the contact stress gradually decreases, resulting in a more stable CoF [37].

All tests displayed the same trend described above (the full set of results is reported in Fig. S7) and the overall CoF of the M2 coating was found to be in the range of 0.45–0.75, which is consistent with previous studies [38].

After testing, the wear tracks were examined using a digital microscope. Fig. 8 displays the three-dimensional profiles of the wear tracks observed on coatings #5 and #8. Although neither sample exhibited a maximum wear depth exceeding 3.2 μm, there is a notable difference in the wear scar area between the two. Sample #8 exhibits a wear scar area of approximately 605.72 μm^2, whereas sample #5 only shows an area of 212 μm^2. These findings underscore the significant impact of the process parameters on the wear resistance of the coatings under examination.

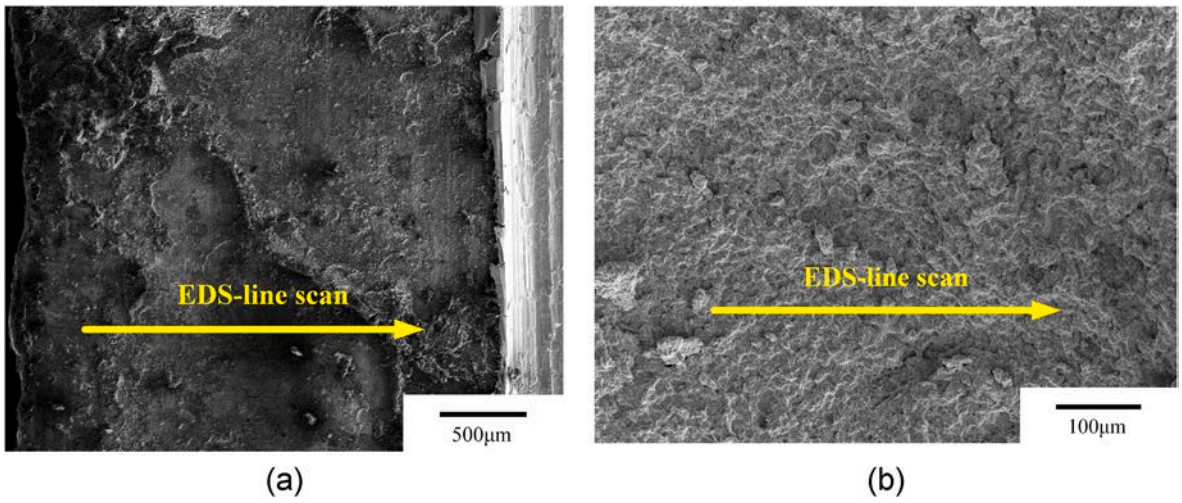

Fig. 6. SEM micrograph and EDS line scans of sample (a) #4 and (b) #14.

Table 4
Chemical compositions of samples #4 and #14 (wt%).

Element	C	O	V	Cr	Fe	Mo	W
Sample #4	27.25	24.53	0.15	3.15	33.86	2.44	1.06
Sample #14	5.46	0.98	3.44	4.55	64.89	6.82	11.01

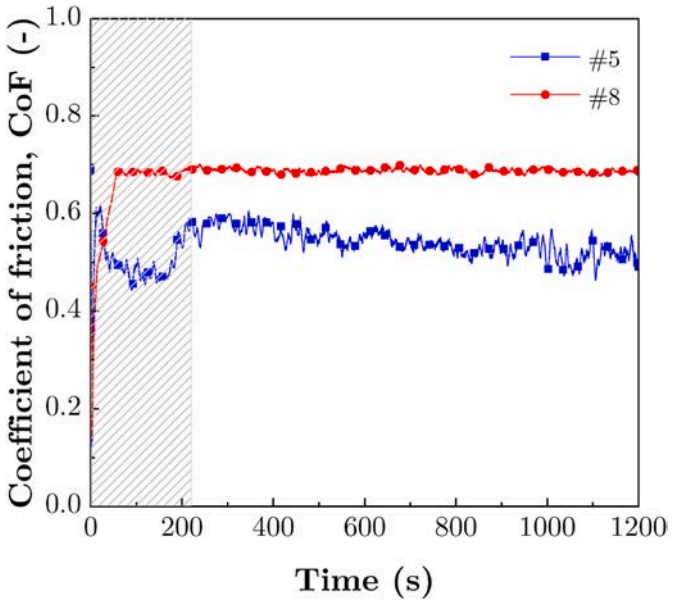

Fig. 7. Typical results of dry sliding frictional tests.

SEM observations of the wear track are presented in Fig. 9. The full set is reported in Fig. S8. Notice that the 16 groups of process parameters were sorted according to the sequence of coating wear scar area results from largest to smallest, and then six samples, i.e., #5, #15, #14, #4, #11, and #8, were selected for further testing. The surface of the wear track, often referred to as the tribo-layer, is formed due to the accumulation of worn particles entrapped at the interface and the extensive deformation caused by tangential stresses during the sliding of the grinding ball. This deformation is particularly apparent in Fig. 9(b), where a plethora of worn particles and peeling pits are evident on the wear track's surface. Furthermore, the presence of numerous particles and shallow furrows on the worn surface of M2 (as depicted in Fig. 9(b)) strongly indicates that the primary wear mechanism at play is abrasion wear [14].

Fig. 10 display the results of EDS scans at three characteristic points under the wear track, which are highlighted in black in Fig. 9(b). From the EDS results, it can be observed that the dark regions (P2) exhibit higher oxygen content, indicating the presence of an oxide layer. This suggests that the coating undergoes some degree of oxidative wear. Similarly, there is (slightly higher) oxygen content in the wear debris (P1), which may be attributed to the oxidation of the wear debris itself. In addition, it can be seen from Fig. S8 that the width of wear scars is different. Coatings with good friction performance have narrower wear scars, and the proportion of oxidation wear is greater, which will be discussed in detail in future studies.

Furthermore, the wt. % of each element is included within Fig. 10. The results reveal that the coating contains high levels of W, Mo, and a certain amount of V. It has been reported that the ratio and types of complex carbides largely determine the wear resistance of high-speed steel [1,39]. W-rich, Mo-rich, and V-rich carbides are known for their excellent hardness and wear resistance [40]. The abundance of hard elements in M2 allows the formation of carbides with W, Mo, V, etc., which can bear a significant load and protect the coating from deep wear. This property enables the M2 coating to exhibit excellent friction and wear performance.

3.4. ANOVA for signal-to-noise ratio based on Taguchi design

3.4.1. Microhardness

The experimental results for each combination of processing variables can be found in the appendix (see Table S1), while the corresponding *SNR* values are presented in Table 5. It is worth noting that ANOVA requires the responses to adhere to a normal distribution. To assess if this requirement was met, a normal probability test was conducted, and the results indicated that the data follow a normal distribution (see Fig. S9).

Based on the SNR_L results for micro-hardness presented in Table 5, and utilizing Minitab statistical software, the ANOVA results and SNR_L response table for micro-hardness were obtained, as illustrated in Tables 6 and 7, respectively.

The ANOVA results reveal that all four process parameters significantly influence micro-hardness. Specifically, the contributions of SS, LP, PF, and OL process parameters to micro-hardness are found to be 15.98 %, 21.11 %, 11.80 %, and 54.38 %, respectively.

In Table 7, the delta values represent the extent of the influence of different process parameters on micro-hardness and are calculated by finding the difference between the best and worst performance achieved

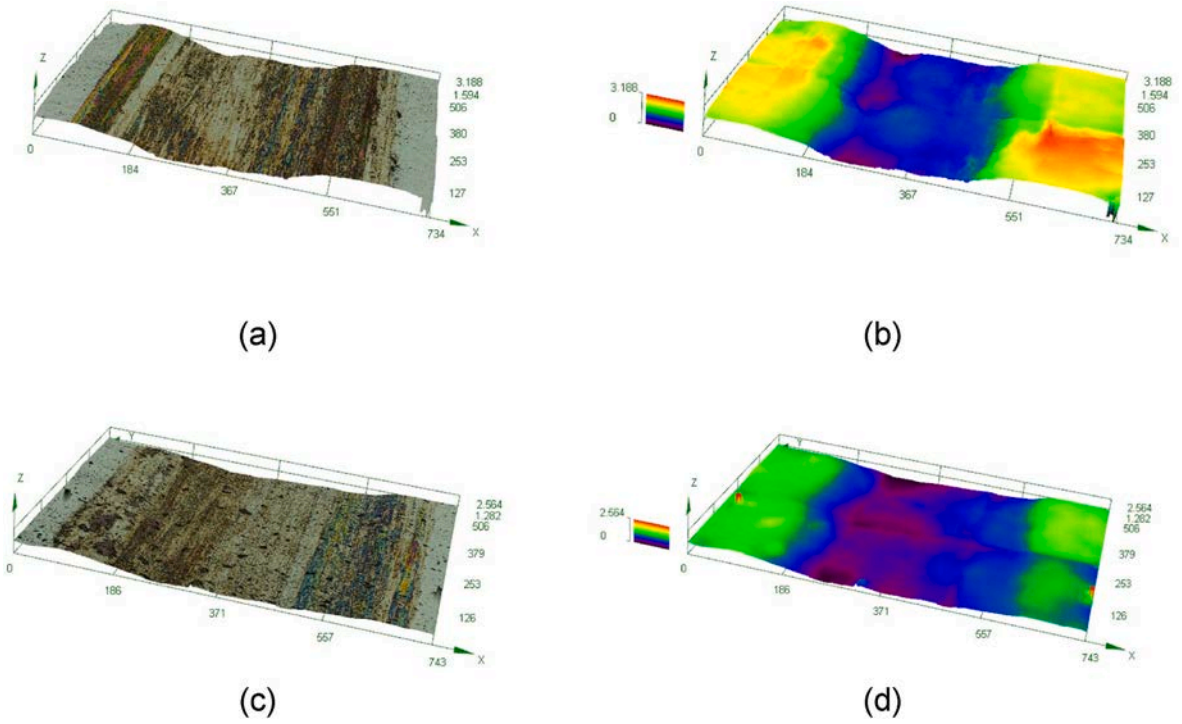

Fig. 8. Three-dimensional wear scar of (a) sample #8 and (c) sample #5; height cloud map of (b) sample #8 and (d) sample #5.

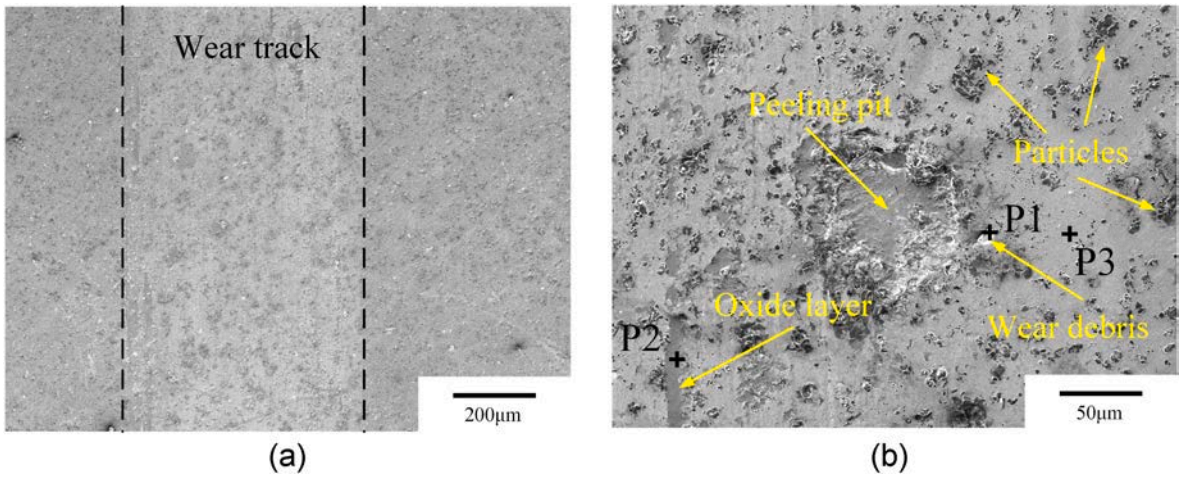

Fig. 9. SEM micrograph of the wear track of sample #8.

for a particular factor level combination. By comparing the magnitudes of delta values, the impact of process parameters on micro-hardness can be ranked. A higher delta value for a process parameter indicates a greater impact on micro-hardness. In Table 7, the process parameters are ranked in the following order based on their influence on micro-hardness: OL > LP > SS > PF.

Fig. 11 presents the main effect plot of SNR_L concerning micro-hardness. The graph showcases a discernible trend where the SNR_L value initially ascends and subsequently descends as the laser power (LP) increases. This pattern finds its roots in the observation that heightened power prompts enhanced M2 powder melting, attaining the pinnacle of melting efficiency at 1600 W.

However, surpassing this threshold could potentially introduce an excessive influx of substrate material into the coating. This abundance of power might contribute to coating softening and foster grain growth, ultimately causing a decline in performance. The SNR_L values fluctuate within a certain range as the SS and PF change, showing no clear pattern. This corresponds to the results in Table 7, where SS and PF have the least impact on micro-hardness. On the other hand, as OL increases, the SNR_L continuously rises. This can be explained because a higher overlapping ratio leads to more laser energy directed to the coating, reducing the melting of the substrate material and limiting its diffusion into the coating.

To investigate the reason for the sharp drop in micro-hardness when LP increased from 1600 W to 1800 W, we conducted microstructural analyses of sample #8 prepared at 1800 W. It was found that compared to sample #11 (LP = 1600 W), sample #8 had a lower content of dendritic structure and carbides, and the grain size was coarser – see Fig. S2 (h). The increase in grain size directly affects the material's strength, leading to softening [41]. Based on the results reported in Fig. 11, the optimal level of parameters that can likely provide the highest micro-hardness is *SS2LP3PF3OL4*.

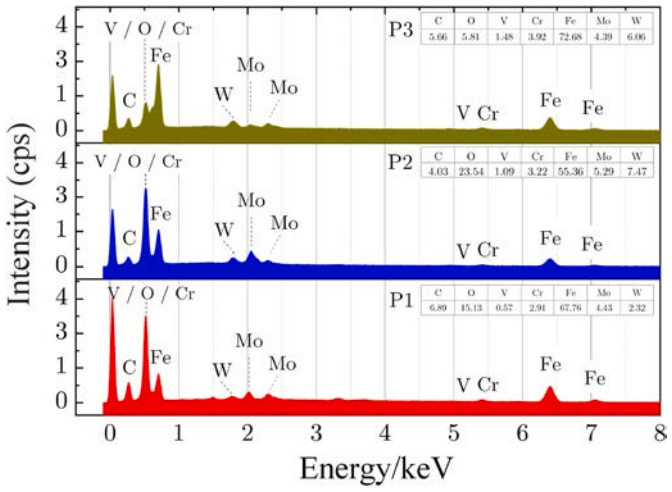

Fig. 10. EDS analysis of wear debris, black regions, and grey regions.

Table 5
Obtained values of the *SNR* for each performance metrics.

Sample #	Bond strength (SNR_L)	CoF (SNR_S)	Wear Scar Area (SNR_S)	Micro-hardness (SNR_L)
1	20.03	5.23	−47.57	56.77
2	21.37	4.14	−52.36	56.85
3	16.76	5.31	−48.67	58.24
4	1.36	3.99	−52.20	57.52
5	20.96	6.06	−46.52	57.12
6	14.18	3.48	−55.30	57.63
7	16.83	5.32	−50.95	57.11
8	17.66	3.34	−55.64	57.17
9	6.52	4.97	−48.46	58.18
10	20.32	3.41	−55.50	57.93
11	24.56	3.60	−53.88	57.77
12	19.30	5.34	−47.75	57.06
13	19.32	4.25	−50.60	57.10
14	25.92	4.93	−48.97	57.28
15	4.76	5.07	−48.35	58.09
16	9.91	3.74	−52.39	57.75

3.4.2. Bond strength

The ANOVA results for bond strength are presented in Table 8, indicating that among the four process parameters, only OL significantly impacts bond strength, while the other three process parameters do not show statistically significant effects. The contributions of SS, LP, PF, and OL to bond strength are 3.89 %, 20.17 %, 2.48 %, and 73.45 %, respectively.

In Table 9, the SNR_L response table for bond strength is displayed. By comparing the delta values, it is evident that the four process parameters are ranked in terms of their influence on bond strength as follows: OL > LP > SS > PF.

Fig. 12 presents the main effect plot of the bond strength SNR_L. The graph reveals that the SNR_L values show an initial increase and then decrease with increasing SS. The variation of SNR_L with PF shows a general downward trend, but with only a slight change in magnitude. Similarly, SNR_L values fluctuate with increasing LP, which aligns with the findings of Karmakar et al. [17], indicating that higher laser power enhances bonding strength. However, excessively high laser power can lead to coating softening and a sharp decrease in bond strength [17]. Furthermore, at lower levels of OL, the change in SNR_L values is not significant. However, at an OL level of 40 %, it is more likely to obtain a coating with good bonding performance. Beyond an OL of 40 %, the SNR_L values sharply decrease because increasing the OL directs more laser energy to the coating than the substrate, weakening the bond between the coating and the substrate. In conclusion, to achieve the best bonding performance between the coating and the substrate, the optimal process parameter selection would be *SS2LP2PF1OL2*.

3.4.3. Coefficient of friction and wear scar area

The ANOVA results for CoF and wear scar area are summarized in Table 10. LP has a significant effect on both CoF and wear scar area, while OL has a significant effect on CoF but not on wear scar area. SS and PF do not show statistical significance in their effects on CoF and wear scar area. The contribution rates of SS, LP, PF, and OL to CoF are 2.16 %, 33.48 %, 27.91 %, and 36.08 %, respectively, and their contribution rates to the wear scar area are 8.46 %, 39.84 %, 26 %, and 27.74 %, respectively.

Table 11 presents the SNR_S response table for CoF and wear scar area. By comparing the delta values, it is evident that the four process parameters are ranked in the following order for their impact on CoF: OL > LP > PF > SS, and for their impact on wear scar area: LP > OL > PF > SS.

Fig. 13(a) and (b) display the main effect plots of CoF and wear scar area SNR_S, respectively. The graphs show that as SS increases, the SNR_S values of both CoF and wear scar area initially decrease and then increase, and the effect is not significant. The other three parameters exhibit consistent effects on both CoF and wear scar area SNR_S. PF shows an increasing trend followed by a decreasing trend for both CoF and wear scar area. On the other hand, LP and OL do not exhibit a clear and distinct pattern of influence on CoF and wear scar area, resulting in significant fluctuations in friction and wear performance within the power range of 1200W–1800W.

This variability in performance can be attributed to the preparation of multi-layered coatings during the friction and wear tests. Notably, when using high power and a high overlapping ratio, the quality of the coatings may be compromised, leading to noticeable defects in some specimens (Fig. S10).

Table 7
Response table for SNR_L of the coating micro-hardness.

Level	SS	LP	PF	OL
1	57.56	57.3	57.49	57.06
2	57.74	57.43	57.28	57.23
3	57.26	57.81	57.72	57.76
4	57.35	57.38	57.42	57.86
Delta	0.48	0.51	0.44	0.81
Rank	3	2	4	1

Table 6
ANOVA results for the coating micro-hardness.

Source		SS	LP	PF	OL	Residual Error	Total
DF		3	3	3	3	3	15
Micro-hardness	Seq SS	0.55	0.61	0.40	1.87	0.01	3.45
	Adj SS	0.55	0.61	0.40	1.87	0.01	
	Adj MS	0.18	0.20	0.13	0.62	0.01	
	F-values	33.86	37.80	25.02	115.25		
	P-values	0.008	0.007	0.013	0.001		
	Contribution	15.98 %	21.11 %	11.80 %	54.38 %		
	Significance	s	s	s	s		

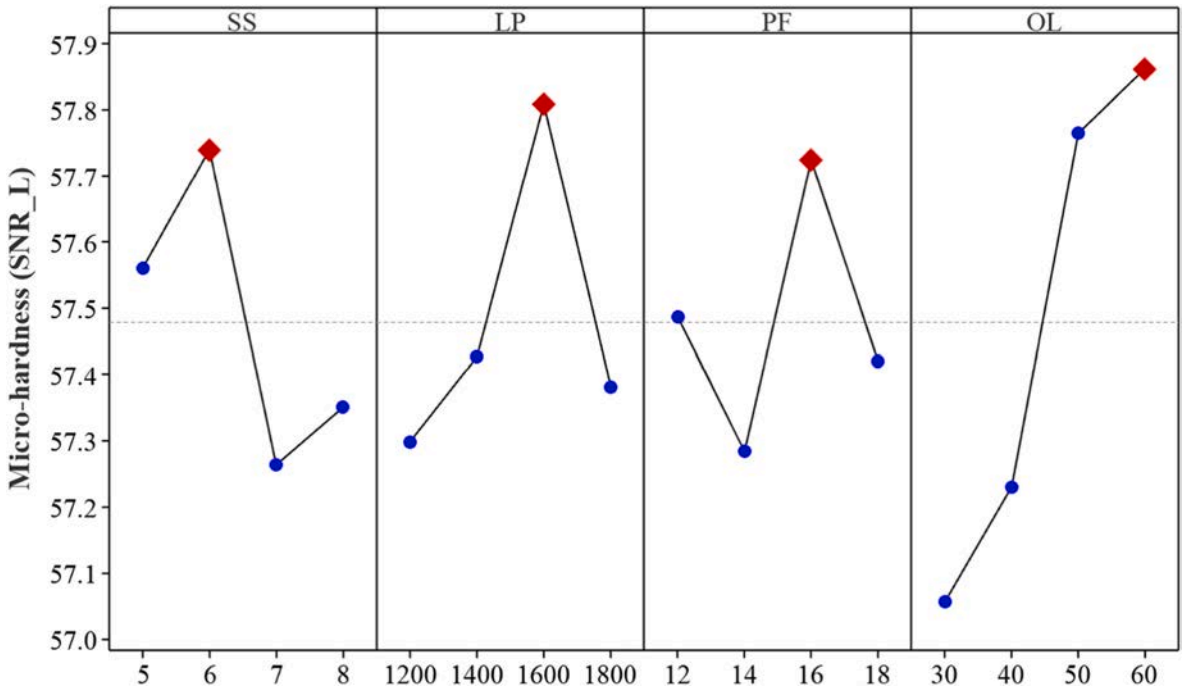

Fig. 11. Main effects plot of the process parameters on the SNR_L of the coating micro-hardness.

Table 8
ANOVA results for the coating bond strength.

Source		SS	LP	PF	OL	Residual Error	Total
DF		3	3	3	3	3	15
Bond strength	Seq SS	27.52	142.77	17.57	519.77	48.51	756.15
	Adj SS	27.52	142.77	17.57	519.77	48.51	
	Adj MS	9.17	47.59	5.85	173.25	16.16	
	F	0.57	2.94	0.36	10.72		
	P	0.671	0.202	0.793	0.041		
	Contribution	3.89 %	20.17 %	2.48 %	73.45 %		
	Significance				s		

Table 9
Response table for SNR_L of the coating bond strength.

Level	SS	LP	PF	OL
1	14.98	16.71	17.17	20.52
2	17.68	20.45	16.60	20.73
3	17.41	15.73	16.71	16.99
4	14.88	12.06	14.46	6.71
Delta	2.79	8.39	2.71	14.02
Rank	3	2	4	1

In conclusion, based on the results reported in Fig. 11 and the evaluation method where higher SNR_S indicates better performance, the optimal process parameters for achieving the best friction and wear performance are *SS4LP1PF2OL1* and *SS1LP1PF2OL1*, respectively.

3.5. Multi-response optimization by TOPSIS-GRA method

The selected parameters combinations outlined in the previous sections do not appear in the originally outlined Taguchi design table. Besides, these combinations do not show agreement for all four responses, i.e., microhardness, bond strength, CoF and wear scar. As a matter of fact, the optimal parameter setting for a particular response might be unfavorable for other responses. To obtain an appropriate combination of processing parameters that can simultaneously satisfy the four responses, i.e., the optimized process parameters, we have adopted the TOPSIS-GRA analysis method. The calculated weights for each response obtained using Eq. (8) are presented in Table 12.

Knowledge of these weights allows to obtain the scores of each alternative (experimental run) using Eq. (12). These scores are subsequently converted into SNR_L. The so-obtained results, along with the rankings for all 16 experiments, are provided in Table 13. A higher SNR_L value indicates that the coating's overall performance for that specific experimental group is superior among the 16 groups. Analyzing Table 13 reveals that sample #4 exhibits the least favorable performance, while sample #5 demonstrates the best performance. It is recalled that the optimal parameters for the fifth experiment are given as: LP = 1200 W, PF = 14 g/min, SS = 7 mm/s, and OL = 50 %.

By combining the single response score with the ANOVA and SNR_L methods, the optimal process parameters for the best overall performance are now determined. Firstly, a normality test was conducted on the scores, and the result (see Fig. S11) indicates a p-value of 0.389, which is greater than 0.05, confirming normality. The SNR_L of the score values determines the quality of the coating's overall performance, where higher values indicate better overall performance.

The ANOVA results for the score are presented in Table 14, where it can be observed that LP and OL significantly influence the overall performance of the coating, while PF and SS do not have statistically significant effects.

The contributions of SS, LP, PF, and OL to the overall performance are 2.28 %, 33.49 %, 23.21 %, and 41.02 %, respectively.

Table 15 presents the response table for SNR_L of the obtained scores

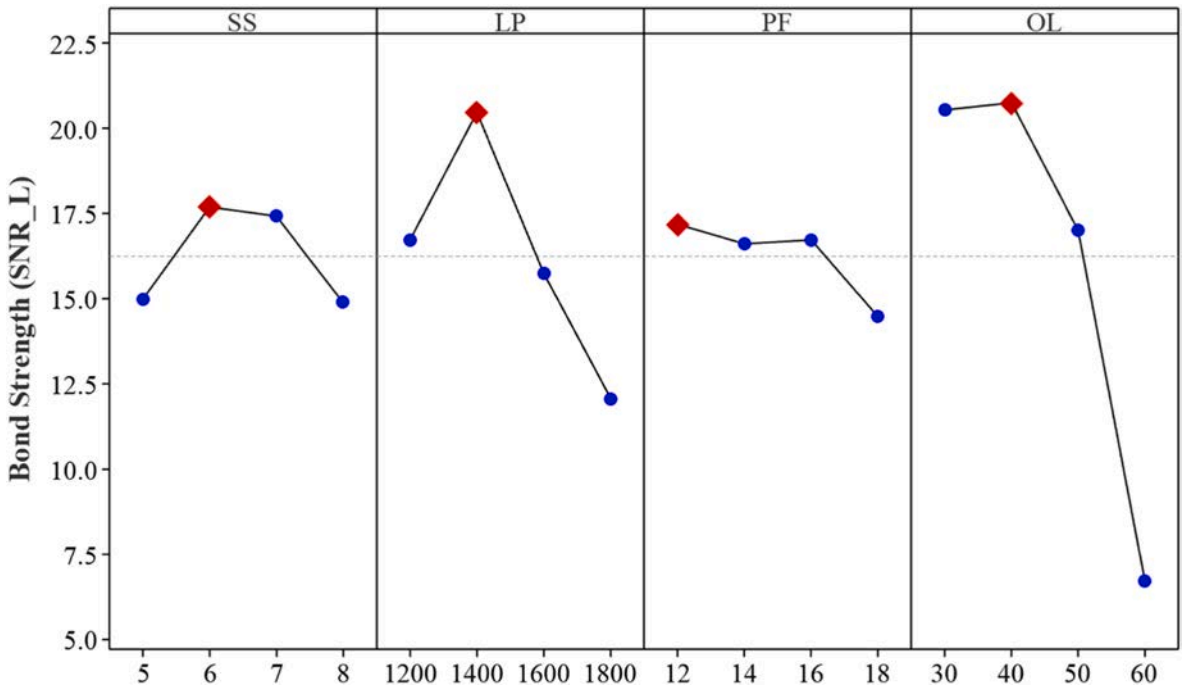

Fig. 12. Main effects plot of the process parameters on the SNR_L of the coating bond strength.

Table 10
ANOVA for CoF and wear scar area.

Source		SS	LP	PF	OL	Residual Error	Total
DF		3	3	3	3	3	15
CoF	Seq SS	0.23	3.65	3.01	3.89	0.35	11.14
	Adj SS	0.23	3.65	3.01	3.89	0.35	
	Adj MS	0.08	1.21	1.01	1.29	0.12	
	F	0.66	10.42	8.59	11.11		
	P	0.620	0.043	0.055	0.039		
	Contribution	2.16 %	33.48 %	27.91 %	36.08 %		
	Significance		s		s		
Wear scar area	Seq SS	11.41	50.96	35.07	37.40	4.47	139.31
	Adj SS	11.40	50.96	35.06	37.39	4.47	
	Adj MS	3.80	16.98	11.6	12.46	1.49	
	F	2.55	11.39	7.84	8.36		
	P	0.231	0.038	0.062	0.057		
	Contribution	8.46 %	39.84 %	26 %	27.74 %		
	Significance		s				

Table 11
Response table for SNR_S of CoF and wear scar area.

Level	CoF				Wear scar area			
	SS	LP	PF	OL	SS	LP	PF	OL
1	4.50	4.01	5.13	5.21	−50.08	−48.29	−52.29	−48.81
2	4.33	5.16	3.99	3.83	−51.4	−53.04	−48.75	−53.13
3	4.55	4.64	4.82	4.63	−52.11	−50.47	−50.44	−50.77
4	4.67	4.24	4.10	4.38	−50.20	−52.00	−52.32	−51.08
Delta	0.33	1.14	1.13	1.37	2.02	4.74	3.57	4.31
Rank	4	2	3	1	4	1	3	2

for each group of experiments. The four process parameters are ranked in the following order based on their impact on the score: OL > LP > PF > SS.

Finally, Fig. 14 shows the main effects plot of the SNR_L of the score. From the plot, it can be observed that as SS increases, the SNR_L of the score initially decreases and then increases, reaching its maximum value at an SS value of 5 mm/s. The LP and OL have a similar impact, both showing a decreasing trend, and the maximum SNR_L of the score is achieved when the LP and OL are at their lowest values, which are 1200 W and 30 %, respectively. The effect of PF initially increases and then decreases, with a maximum obtained at a 14 g/min.

Based on the results, the optimal process parameters for achieving the best overall coating performance are given as follows: SS at 5 mm/s, LP at 1200 W, PF at 14 g/min, and OL at 30 % (*SS1LP1PF2OL1*).

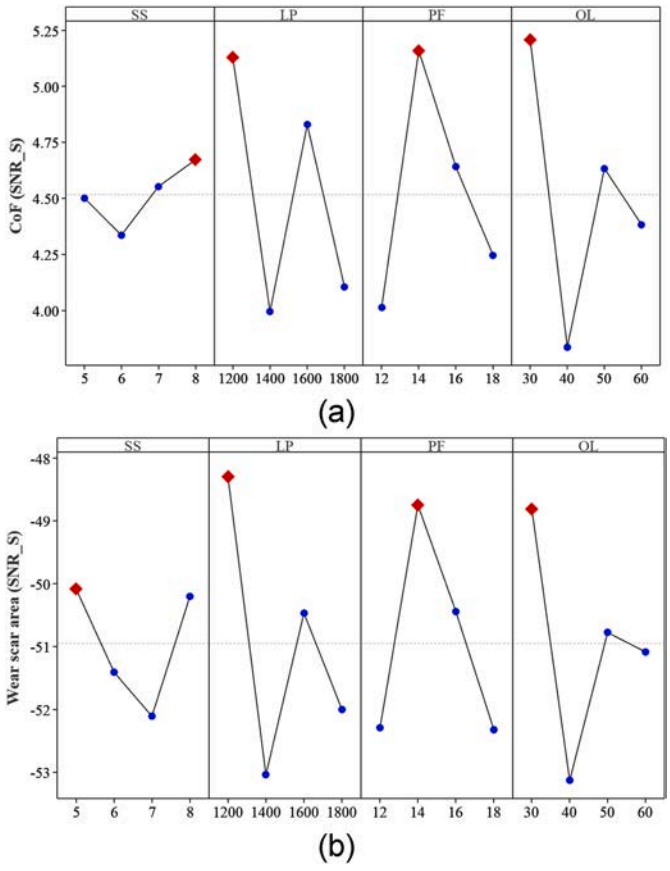

Fig. 13. Main effects plot of the process parameters on the SNR_S of the CoF and the wear scar area.

Table 12
Weights of each response.

	CoF	Wear scar area	Micro-hardness	Bond strength
Weight	0.2655	0.2434	0.2514	0.2397

Table 13
Scores, SNR_L, and rankings for the experimental conditions considered in the study.

Sample #	Score	SNR_L of score	Rank
1	0.81	−1.78	2
2	0.52	−5.56	9
3	0.70	−3.04	5
4	0.26	−11.58	16
5	**0.88**	**−1.10**	**1**
6	0.28	−10.81	15
7	0.57	−4.85	7
8	0.33	−9.42	14
9	0.53	−5.35	8
10	0.38	−8.38	12
11	0.48	−6.26	11
12	0.79	−1.97	3
13	0.60	−4.39	6
14	0.78	−2.06	4
15	0.52	−5.62	10
16	0.34	−9.32	13

3.6. Experimental validation

The coating prepared with the process parameters *SS1LP1PF2OL1* was defined as the optimal combination of processing parameters, and the corresponding measured responses are summarized in Table 16. Notice that such a combination was not included in the original Taguchi table.

Therefore, a comparison was made between the so-obtained optimal solution and the sample that has shown the best performance within the experimental Taguchi table, i.e., sample #5. Such a comparison is illustrated in Fig. 15. It is shown that compared to sample #5, the optimal solution entails larger bond strength (+44 %) and comparable microhardness (+2 %), as well as smaller wear scar area (−5%) and CoF (−7%). Overall, the coating obtained under the optimal parameters are likely to exhibit superior performance compared to the optimal group from the orthogonal experiments.

Further analysis of the microstructure of the 'optimal' coating was conducted using scanning electron microscopy (SEM). The results are presented in Fig. S2 (m) and (n) in the Supplementary Information. Based on the SEM results, we inferred that the process parameters generate a relatively small grain size. Additionally, the shear sample prepared under the optimal parameter set exhibited excellent bond strength. The SEM analysis of fracture surfaces revealed cohesive fractures without exposure of the underlying A2 substrate. A visual example is provided in Fig. S5 (i). Thus, it can be concluded that the metallurgical bond at the coating/substrate interface under the optimal processing set was satisfactory.

Furthermore, friction-wear experiments indicated an extremely narrow width of the wear scar, but a large area of oxidative wear was observed - see Fig. S8 (k).

4. Conclusions

The study investigated the effects of laser power, scan speed, powder feeding rate, and overlapping ratio on the micro-hardness, friction and wear performance, and bond strength between M2 coating and substrate using orthogonal experimental design, *SNR*, and ANOVA methods. The microstructural factors affecting the coating's performance were also examined from a microscopic perspective. Moreover, a comprehensive evaluation of the coating performance for each group of samples was achieved through the combination of grey relational analysis and the TOPSIS algorithm. The optimal process parameters were identified and then validated through experimental testing. Based on the research findings, the following conclusions were drawn:

1. The micro-hardness of the M2 coating exhibited a significant improvement, increasing by 3–4 times compared to the A2 substrate. All four process parameters demonstrated a significant impact on micro-hardness. Notably, the overlapping ratio had the most substantial influence, contributing to 54.38 % of the variation in micro-hardness. The high micro-hardness of the M2 coating can be attributed to the presence of fine carbide networks, a significant amount of hard elements such as V and W, and precipitated carbides. Increasing the laser power facilitated sufficient powder melting, enhancing the micro-hardness of the coating. However, it is important to avoid excessively high laser power, as it can lead to grain growth and reduce the micro-hardness.
2. Among the factors considered, only the overlapping ratio demonstrated a substantial impact on bond strength, accounting for a significant 73.45 % contribution rate. The low maximum shear force observed can be attributed to improper process parameter selection, where a high overlapping ratio led to a concentration of laser energy on the powder, resulting in inadequate substrate melting. Consequently, the desired strong metallurgical bond between the coating and substrate failed to form. This deficiency manifested in a brittle fracture mode, as indicated by the presence of cleavage steps and river patterns, which provide evidence of a cleavage fracture mechanism.
3. Laser power had the greatest influence on frictional performance, while the overlapping ratio had the greatest influence on wear

Table 14
ANOVA for the obtained scores.

Source		SS	LP	PF	OL	Residual Error	Total
DF		3	3	3	3	3	15
Micro-hardness	Seq SS	3.72	54.69	37.89	66.97	5.22	168.51
	Adj SS	3.72	54.69	37.89	66.97	5.22	
	Adj MS	1.24	18.23	12.63	22.32	1.74	
	F	0.71	10.47	7.25	12.82		
	P	0.606	0.043	0.069	0.032		
	Contribution	2.28 %	33.49 %	23.21 %	41.02 %		
	Significance		s		s		

Table 15
Response table for SNR_L of score.

Level	SS	LP	PF	OL
1	−5.35	−3.16	−7.04	−2.66
2	−5.49	−6.70	−3.56	−6.41
3	−6.55	−4.94	−4.97	−5.46
4	−5.49	−8.07	−7.30	−8.34
Delta	1.20	4.91	3.74	5.67
Rank	4	2	3	1

performance. However, at high laser power and overlapping ratio, the coating's surface quality deteriorated, making it difficult to observe a clear influence of process parameters on friction and wear performance. The excellent friction and wear performance of the M2 coating can be attributed to the presence of W-rich, Mo-rich, and V-rich carbides. The dominant wear mechanism of the coating was abrasive wear, with some evidence of oxidation wear.

4. The optimal group of experiments based on the TOPSIS-GRA method was identified as the fifth group. Through ANOVA and *SNR* analysis of the scores of each experiment, the optimal process parameters were determined to be: a scan speed of 5 mm/s, a laser power of 1200 W, a powder feeding rate of 14 g/min, and an overlapping ratio of 30 %. The coating prepared with these optimal process parameters was subjected to validation experiments, and the results showed that the bond strength, wear scar area, and coefficient of friction of the coating were 16.142 kN, 0.4647, 201.37 μm^2, and 734.22 $HV_{0.5}$, respectively. All these performance metrics were superior to those obtained from the fifth group of experiments.

Author contributions

Heran Geng: Methodology, Validation, Investigation, Writing – original draft. **Marco Alfano:** Writing – review & editing, Supervision. **Junfeng Yuan:** Supervision, Resources, Project administration.

Funding

This work was supported by grants from the China Postdoctoral Science Foundation Funded Project (No. 2021M693415), the China Postdoctoral International Exchange Program (Project No. PC2022061), the National Science Fund for Excellent Young Scholars (Oversea), the Jiangsu Provincial Postdoctoral Science Foundation Funded Project (No. 2020C340), the Postgraduate Innovation Program of the China University of Mining and Technology (No. 2023WLJCRCZL110), and the Jiangsu Provincial Double-Innovation Doctor Program (No. 202031063), M.A. gratefully acknowledges financial support received

Table 16
Coating performance under optimal process parameters.

Bond strength (kN)	CoF	Wear scar area (μm^2)	Micro-hardness ($HV_{0.5}$)
16.14	0.46	201.37	734.22

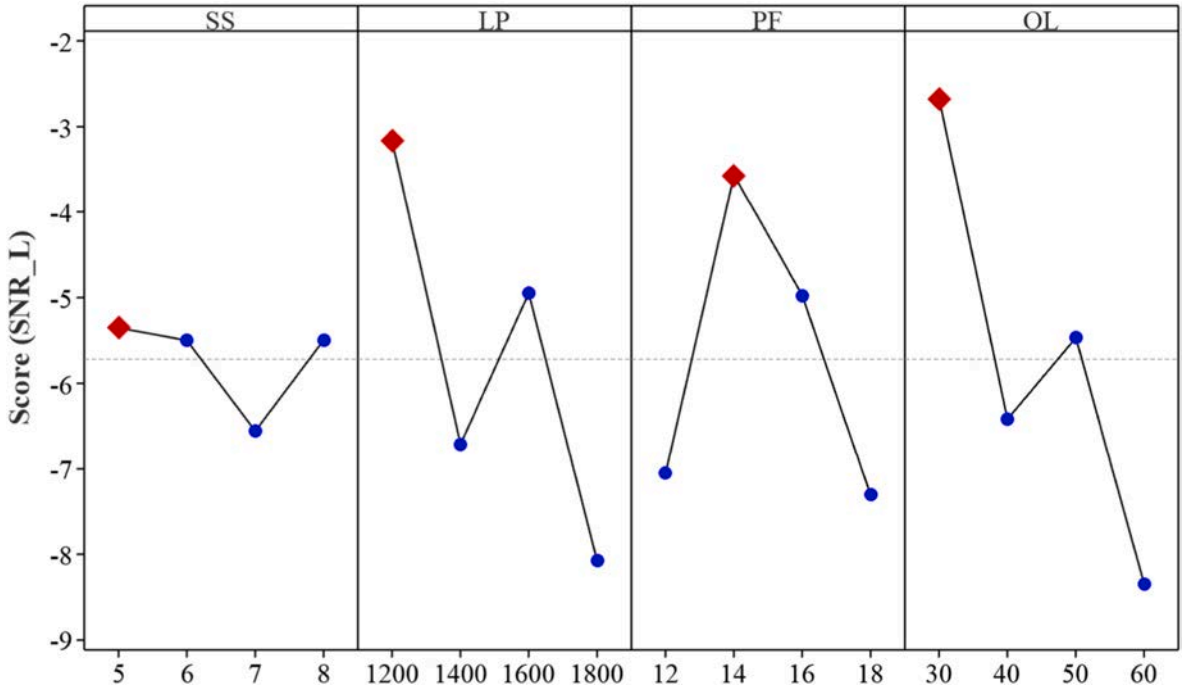

Fig. 14. Main effects plot of the process parameters on the SNR_L of the score.

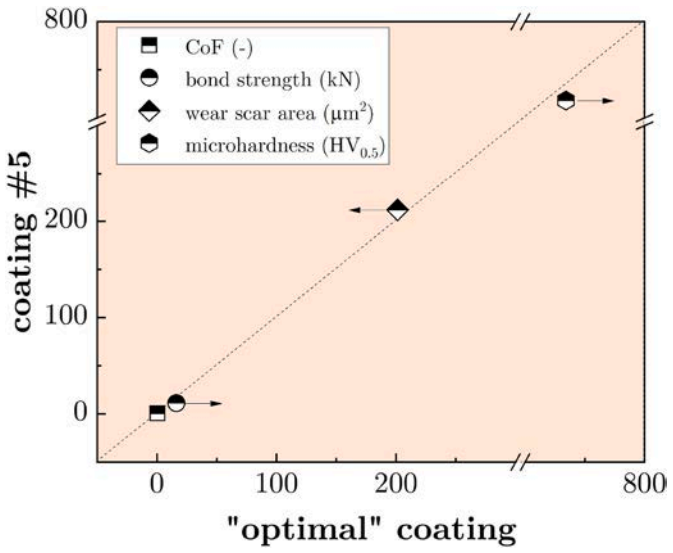

Fig. 15. Performance comparison between the validation group and sample #5.

from University of Waterloo (Starter Grant).

Declaration of competing interest

We declare that we have no known competing financial interests or personal relationships that could have appeared to influence the work reported in this paper.

Appendix A. Supplementary data

Supplementary data to this article can be found online at https://doi.org/10.1016/j.jmrt.2024.01.087.

References

[1] Navas C, Conde A, Fernández B, Zubiri F, De Damborenea J. Laser coatings to improve wear resistance of mould steel. Surf Coat Technol 2005;194:136–42. https://doi.org/10.1016/j.surfcoat.2004.05.002.
[2] Ju J, Zhou Y, Kang M, Wang J. Optimization of process parameters, microstructure, and properties of laser cladding fe-based alloy on 42CrMo steel roller. Materials 2018;11:2061. https://doi.org/10.3390/ma11102061.
[3] Padmanabham G, Bathe R. Laser materials processing for industrial applications. Proc Natl Acad Sci India A 2018;88:359–74.
[4] Guo C, Zhou J, Zhao J, Wang L, Yu Y, Chen J, Zhou H. Improvement of the oxidation and wear resistance of pure Ti by laser-cladding Ti 3 Al coating at elevated temperature. Tribol Lett 2011;42:151–9. https://doi.org/10.1007/s11249-011-9756-z.
[5] Liu XB, Meng XJ, Liu HQ, Shi GL, Wu SH, Sun CF, Wang MD, Qi LH. Development and characterization of laser clad high temperature self-lubricating wear resistant composite coatings on Ti-6Al-4V alloy. Mater Des 2014;55:404–9. https://doi.org/10.1016/j.matdes.2013.09.038.
[6] Song MJ, Wu LS, Liu JM, Hu Y. Effects of laser cladding on crack resistance improvement for aluminum alloy used in aircraft skin. Opt Laser Technol 2021;133:106531. https://doi.org/10.1016/j.optlastec.2020.106531.
[7] Lian G, Xiao S, Zhang Y, Jiang J, Zhan Y. Multi-objective optimization of coating properties and cladding efficiency in 316L/WC composite laser cladding based on grey relational analysis. Int J Adv Manuf Technol 2021;112:1449–59. https://doi.org/10.1007/s00170-020-06486-1.
[8] Xi W, Song B, Wang Z, Yu T, Wang J, Dai Y. Effect of laser re-melting on geometry and mechanical properties of YCF102 cladding layer. Surf Coat Technol 2021;408:126789. https://doi.org/10.1016/j.surfcoat.2020.126789.
[9] Yuan W, Li R, Chen Z, Gu J, Tian Y. A comparative study on microstructure and properties of traditional laser cladding and high-speed laser cladding of Ni45 alloy coatings. Surf Coat Technol 2021;405:126582. https://doi.org/10.3390/ma15186400.
[10] Lin Y, Jiang C, Lin Z, Chen Q, Lei Y, Fu H. Laser in-situ synthesis of high aspect ratio TiB fiber bundle reinforced titanium matrix composite coating. Opt Laser Technol 2019;115:364–73. https://doi.org/10.1016/j.optlastec.2019.02.047.
[11] Yu Y, Zhou J, Chen J, Zhou H, Guo C, Wang L, Yang L. Preparation, microstructure and tribological behavior of laser cladding NiAl intermetallic compound coatings. Wear 2012;274:298–305. https://doi.org/10.1016/j.wear.2011.09.011.
[12] Lian G, Zhang H, Zhang Y, Yao M, Huang X, Chen C. Computational and experimental investigation of micro-hardness and wear resistance of Ni-based alloy and TiC composite coating obtained by laser cladding. Materials 2019;12:793. https://doi.org/10.3390/ma12050793.
[13] Fais A, Maizza G. Densification of AISI M2 high speed steel by means of capacitor discharge sintering (CDS). J Mater Process Technol 2008;202:70–5. https://doi.org/10.1016/j.jmatprotec.2007.09.012.
[14] Wang L, Yang J-h, Li Y, Song J, Jin Y-x, Wang S-q. Wear behavior of TC11 and AISI M2 in pin–disk tribo-system. J Iron Steel Res Int 2019;26:490–500. https://doi.org/10.1007/s42243-019-00246-6.
[15] Bax B, Rajput R, Kellet R, Reisacher M. Systematic evaluation of process parameter maps for laser cladding and directed energy deposition. Addit Manuf 2018;21:487–94. https://doi.org/10.1016/j.addma.2018.04.002.
[16] Aghili SE, Shamanian M. Investigation of powder fed laser cladding of NiCr-chromium carbides single-tracks on titanium aluminide substrate. Opt Laser Technol 2019;119:105652. https://doi.org/10.1016/j.optlastec.2019.105652.
[17] Karmakar DP, Muvvala G, Nath AK. Effect of scan strategy and heat input on the shear strength of laser cladded Stellite 21 layers on AISI H13 tool steel in as-deposited and heat treated conditions. Surf Coat Technol 2020;384:125331. https://doi.org/10.1016/j.surfcoat.2019.125331.
[18] Xu Z, Yuan J, Wu M, Arif AFM, Li D. Effect of laser cladding parameters on Inconel 718 coating performance and multi-parameter optimization. Opt Laser Technol 2023;158:108850. https://doi.org/10.1016/j.optlastec.2022.108850.
[19] Mondal S, Paul C, Kukreja L, Bandyopadhyay A, Pal PK. Application of Taguchi-based gray relational analysis for evaluating the optimal laser cladding parameters for AISI1040 steel plane surface. Int J Adv Manuf Technol 2013;66:91–6. https://doi.org/10.1007/s00170-012-4308-8.
[20] Lian G, Zhang H, Zhang Y, Tanaka ML, Chen C, Jiang J. Optimizing processing parameters for multi-track laser cladding utilizing multi-response grey relational analysis. Coatings 2019;9:356. https://doi.org/10.3390/coatings9060356.
[21] Hao X, Li M, Chen Y. China's overcapacity industry evaluation based on TOPSIS grey relational projection method with mixed attributes. Grey Syst 2021;11:288–308. https://doi.org/10.1108/gs-03-2020-0033.
[22] Hui G, Bifeng S. Study on effectiveness evaluation of weapon systems based on grey relational analysis and TOPSIS. J Syst Eng Electron 2009;20:106–11.
[23] Yang W, Wu Y. A novel TOPSIS method based on improved grey relational analysis for multi-attribute decision-making problem. Math Probl Eng 2019;2019. https://doi.org/10.1155/2019/8761681.
[24] Blakely M, Pauly S, Prothe C. Design considerations in Attaching pressure vessel internals: welding to the pressure boundary or welding to the clad? ESOPE 2016.
[25] Martin Vinoth S, Dinesh Babu P, Marimuthu P, Phalke SS. Laser cladding of nickel powder on AISI 202 stainless steel and optimization of the process parameters. In: Advances in manufacturing processes. Singapore: Springer; 2019. p. 197–203. https://doi.org/10.1007/978-981-13-1724-8_19.
[26] Hussain M, Kumar V, Mandal V, Singh PK, Kumar P, Das AK. Development of cBN reinforced Ti6Al4V MMCs through laser sintering and process optimization. Mater Manuf Process 2017;14:1667–77. https://doi.org/10.1080/10426914.2017.1303152.
[27] Shi KN, Zhang DH, Ren JX. Optimization of process parameters for surface roughness and microhardness in dry milling of magnesium alloy using Taguchi with grey relational analysis. Int J Adv Manuf Technol 2015;1–4:645–51. https://doi.org/10.1007/s00170-015-7218-8.
[28] Maheswaran C, Bharathi RJ, Srirangan AK. Optimisation of laser welding parameters for incoloy 800HT joints using Grey-fuzzy Taguchi approach. Mater Today Proc 2018;5:14237–43. https://doi.org/10.1016/j.matpr.2018.03.004.
[29] Prakash KS, Gopal P, Karthik S. Multi-objective optimization using Taguchi based grey relational analysis in turning of Rock dust reinforced Aluminum MMC. Measurement 2020;157:107664. https://doi.org/10.1016/j.measurement.2020.107664.
[30] Yu TB, Yang L, Zhao Y, Sun JY, Li BC. Experimental research and multi-response multi-parameter optimization of laser cladding Fe313. Opt Laser Technol 2018;108:321–32. https://doi.org/10.1016/j.optlastec.2018.06.030.
[31] de Almeida EdS, Krelling A, Milan J, da Costa C. Micro-abrasive wear mechanisms of P/M AISI M2 steel with different surface treatments. Surf Coat Technol 2018;333:238–46. https://doi.org/10.1016/j.surfcoat.2017.10.020.
[32] Pellizzari M, Zadra M, Fedrizzi A. Development of a hybrid tool steel produced by spark plasma sintering. Mater Manuf Process 2009;24:873–8. https://doi.org/10.1080/10426910902917504.
[33] Baek GY, Shin GY, Lee EM, Shim DS, Lee KY, Yoon H-S, Kim MH. Mechanical characteristics of a tool steel layer deposited by using direct energy deposition. Met. Mater.-Int. 2017;23:770–7. https://doi.org/10.1007/s12540-017-6442-1.
[34] Darmawan W, Quesada J, Rossi F, Marchal R, Machi F, Usuki H. Performance of laser-treated AISI-M2 cutting tools for peeling beech. Eur. J. Wood Wood Prod. 2009;67:247–55. https://doi.org/10.1007/s00107-009-0324-2.
[35] Onuike B, Bandyopadhyay A. Functional bimetallic joints of Ti6Al4V to SS410. Addit Manuf 2020;31:100931. https://doi.org/10.1016/j.addma.2019.100931.
[36] Reichardt A, Dillon RP, Borgonia JP, Shapiro AA, McEnerney BW, Momose T, Hosemann P. Development and characterization of Ti-6Al-4V to 304L stainless steel gradient components fabricated with laser deposition additive manufacturing. Mater Des 2016;104:404–13. https://doi.org/10.1016/j.matdes.2016.05.016.
[37] Bai Q, Ouyang C, Zhao C, Han B, Liu Y. Microstructure and wear resistance of laser cladding of Fe-based alloy coatings in different areas of cladding layer. Materials 2021;14:2839. https://doi.org/10.3390/ma14112839.
[38] Oliveira CKNd, Riofano RM, Casteletti LC. Micro-abrasive wear test of niobium carbide layers produced on AISI H13 and M2 steels. Surf Coat Technol 2006;200:5140–4. https://doi.org/10.1016/j.surfcoat.2005.05.037.

[39] Wang S-H, Chen J-Y, Xue L. A study of the abrasive wear behaviour of laser-clad tool steel coatings. Surf Coat Technol 2006;200:3446–58. https://doi.org/10.1016/j.surfcoat.2004.10.125.

[40] Trtica MS, Gaković BM, Nenadović TM, Mitrović MM. Surface modification of stainless steels by TEA CO2 laser. Appl Surf Sci 2001;177:48–57. https://doi.org/10.1016/s0169-4332(01)00208-2.

[41] Cordero ZC, Knight BE, Schuh CA. Six decades of the Hall–Petch effect–a survey of grain-size strengthening studies on pure metals. Int Mater Rev 2016;61:495–512. https://doi.org/10.1080/09506608.2016.1191808.